Mathematical and Computational Applications

MDPI

Article

A Time-Domain Artificial Boundary for Near-Field Wave Problem of Fluid Saturated Porous Media

Jia Song [1,2,*], Fujie Wang [1], Kemin Jia [2] and Haohao Shen [1]

[1] School of Civil Engineering, North China University of Technology, Beijing 100144, China
[2] Key Laboratory of Urban Security and Disaster Engineering, Ministry of Education, Beijing University of Technology, Beijing 100124, China
* Correspondence: sjandrew@163.com

Abstract: The near-field wave problem of the saturated soil involves the energy radiation effect of the truncated infinite media. A viscous spring boundary is proposed for the fluid-saturated porous media. Based on the process of wave propagation under internal point source, the stress and flow velocity boundaries are constructed by reasonable assumptions of outgoing waves and Green's function, respectively. Without the permeability assumption, the proposed boundary avoids the low accuracy caused by the assumption of zero permeability that is widely used in the existing methods. The boundary simultaneously has a simple form, clear physical meaning, and less computational cost due to its local character. Meanwhile, a completely explicit integration algorithm considering the damping is constructed to solve the finite element equations of saturated porous media with the proposed boundary. The accuracy and high computational efficiency of the wave numerical method are verified in the examples.

Keywords: fluid-saturated porous media; ***u***-*p* formulation; viscous spring artificial boundary; explicit integration algorithm; Green's function

Citation: Song, J.; Wang, F.; Jia, K.; Shen, H. A Time-Domain Artificial Boundary for Near-Field Wave Problem of Fluid Saturated Porous Media. *Math. Comput. Appl.* **2022**, *27*, 71. https://doi.org/10.3390/mca27040071

Academic Editor: Zhuojia Fu

Received: 10 July 2022
Accepted: 16 August 2022
Published: 18 August 2022

1. Introduction

The wave problem of saturated two-phase porous media is an important research issue of soil dynamics and geotechnical seismic engineering. For the problem, Biot [1] established the three-dimensional quasi-static consolidation theory by considering the deformation of solid and liquid phases, as well as the fluid-solid coupling of saturated porous media. Based on this, Biot wave theory is proposed by adding the inertial terms of soil skeleton and pore fluid [2,3]. However, there are several elastic coefficients with relatively abstract meanings in the equations, and the concept of additional mass density describing the coupling of solid and fluid lacks physical meaning, which makes it relatively difficult to measure. Therefore, many scholars improved Biot theory furtherly [4–7]. The dynamic equations proposed by Zienkiewicz [7,8] is essentially equivalent to the Biot theory. In the equations, the additional mass density is ignored and assumes that dynamic permeability coefficient considers the fluid viscosity. Men et al. [9] and Chen et al. [10] considered the incompressibility and compressibility of the pore fluid, respectively, and gave the dynamic governing equations for saturated porous media under the two conditions. Wu [11] compared the dynamic equations proposed by Biot theory and Zienkiewicz, proved that the two equations are equivalent, and gave the corresponding relationships between the corresponding parameters. Zhao et al. [12] used inductive and deductive methods to review the existing wave theory of porous media. Morency and Tromp [13] presents a numerical implementation of poroelastic wave propagation using a spectral element method, based upon an averaging technique which accommodates the transition from the microscopic to the macroscopic scale. Puente and Dumbser [14] introduced a local space-time discontinuous Galerkin method with arbitrary high-order accuracy to simulate wave propagation in poroelastic material. Wang et al. [15] investigated the wave propagation in 2D periodic fluid-saturated porous media with an isotropic or a transversely isotropic matrix.

For the near-field wave problems, absorbing artificial boundary are needed to model waves propagation in infinite field, to ensure waves have no reflection effect when passing through the artificial boundary [16]. The wave transmission boundary mainly includes [17] global precise artificial boundaries [18–20] and local artificial boundaries [21–27]. The global artificial boundary mainly includes boundary element method [28], thin layer method [29], exact Kirchhoff integration method [18,19] and Dirichlet-to-Neumann method [20,30]. The boundary conditions are established based on the initial boundary value conditions of the truncated media and are gotten through rigorous analytical derivation, leading to complicated calculation process and low efficiency. Local artificial boundaries include the viscous boundaries [21,31], the viscous-spring boundaries [22–24,32–35], the superposition boundaries [25,36], the extrapolation boundaries [26,37], the paraxial boundaries [38,39], the multi-directional boundary [27,40], the perfectly matched layer [41,42], and the dynamic infinite element [43–45]. The local artificial boundary is local both in space and time domain, that is, the responses of the target node are only related to the responses of the adjacent nodes. It has less calculation amount and higher calculation efficiency.

For the fluid saturated porous media, Modaressi and Benzzenati [46,47] established paraxial boundaries for the $\boldsymbol{u}$-p formulation and obtained the zero-order and first-order paraxial boundary conditions, where the zero-order paraxial boundary is equivalent to the viscous boundary. Akiyoshi et al. [48] established paraxial boundaries for the u-w, u-U, and $\boldsymbol{u}$-p models of linear and isotropic saturated soils, and extended their work to the case of laterally isotropic and anisotropic saturated soils [49,50]. The above research work is based on plane waves. Liu Guanglei and Song Erxiang [51] prop osed a viscous spring artificial boundary for the $\boldsymbol{u}$-p equation based on cylindrical waves. Du Xiuli et al. [52] and Zhao Chenggang et al. [53,54] established two viscous spring artificial boundaries based on u-U formulation. To improve the accuracy of artificial boundaries, Li Peng and Song Erxiang [55] proposed a new high-precision artificial boundary on the basis of the work of Song Erxiang [51]. Degrande and De Roeck [56,57] proposed a global artificial boundary in the frequency domain, but its computational cost is higher. Then, under the assumptions of zero and infinity permeability coefficient, Gajo et al. [58] as well as Zerfa and Loret [59] established, respectively, two viscous boundary conditions with high computational efficiency in the time domain.

The assumption of permeability coefficient leads to neglect of fluid-solid coupling, resulting in the low accuracy of dynamic responses of the fluid saturated porous media. A new viscous spring artificial boundary without the permeability coefficient assumption is proposed based on the $\boldsymbol{u}$-p equation of the saturated porous media. Green's function is firstly used to establish the flow boundary velocity condition due to the similar principle by describing the pore pressure field generated by the point force. A completely explicit integration algorithm considering the damping is constructed to solve the finite element equations of saturated porous media with the proposed boundary. Finally, three examples are used to show the accuracy and effectiveness of the proposed method by comparing with analysis solutions and numerical solutions of existing boundary.

2. Wave Velocity

The propagation of waves in the semi infinitely field of saturated soil under point force is shown in Figure 1, which can be described by $\boldsymbol{u}$-p equation. Ignoring the body force, the $\boldsymbol{u}$-p formed control equations of fluid-saturated porous media are expressed as:

$$(\lambda + G)\nabla\nabla \cdot \boldsymbol{u} + G\nabla^2\boldsymbol{u} - \alpha\nabla p = \rho\ddot{\boldsymbol{u}} \tag{1}$$

$$k_f\nabla^2 p - \alpha\nabla \cdot \dot{\boldsymbol{u}} = \frac{1}{Q_b}\dot{p} \tag{2}$$

where λ and G are the Lamb constants of the soil. α and Q_b are the compressive coefficient of the soil skeleton and pore fluid, respectively. k_f is the dynamic permeability coefficient. ρ represents the density of the total solid-fluid mixture. $\nabla^{\mathrm{T}} = [\partial/\partial x \quad \partial/\partial y]$. $\boldsymbol{u}$ and p represent the displacement and pore pressure of saturated soil, respectively.

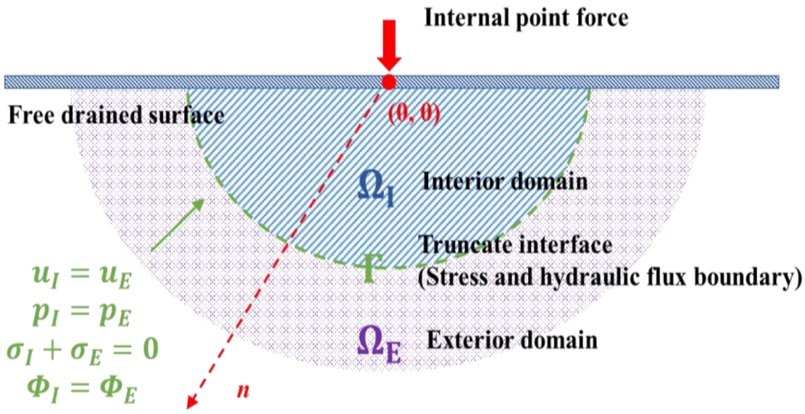

Figure 1. Schematic diagram of the wave in a saturated soil field under an interior point force.

Equations (1) and (2) are further transformed into the frequency domain, and the following equations are obtained by introducing the parameter $\rho_{m1} = -\frac{1}{k}\frac{i}{\omega}$:

$$(\lambda + G)\nabla\nabla \cdot \boldsymbol{u} + G\nabla^2\boldsymbol{u} + \omega^2\rho\boldsymbol{u} - \alpha\nabla p = \boldsymbol{0} \tag{3}$$

$$\nabla^2 p + \frac{\omega^2\rho_m}{Q_b}p + \omega^2\alpha\rho_m\nabla \cdot \boldsymbol{u} = 0 \tag{4}$$

where ω represents the circular frequency, and the displacement and pore pressure are expressed by the rotational and irrotational potential functions of $P1$, $P2$, and S waves as shown in Equations (5) and (6):

$$\boldsymbol{u} = \nabla\varphi_{P1} + \nabla\varphi_{P2} + \nabla \times \psi_s\boldsymbol{e} \tag{5}$$

$$p = (\eta_1 - \alpha Q_b)\nabla^2\varphi_{P1} + (\eta_2 - \alpha Q_b)\nabla^2\varphi_{P2} \tag{6}$$

where φ_{P1} and φ_{P2} represent the potential function of $P1$ and $P2$ waves, respectively; ψ_s represents the potential function of S wave; $\boldsymbol{e}$ is the unit vector. At the same time, η_1 and η_2 in Equation (6) are calculated as shown:

$$\eta_{1,\,2} = \frac{\alpha Q_b}{\rho_{m1}V_{P1,\,P2}^2 - Q_b} \tag{7}$$

Substituting Equations (5) and (6) into Equations (3) and (4), the wave equations expressed by the potential functions of $P1$, $P2$, and S waves are obtained as follows:

$$V_{P1,\,P2}^2\nabla^2\varphi_{P1,\,P2} + \omega^2\varphi_{P1,\,P2} = 0 \tag{8}$$

$$V_S^2\nabla^2\psi_S + \omega^2\psi_S = 0 \tag{9}$$

where, V_{P1}, V_{P2}, and V_S, shown in Equation (10), are the nominal wave velocity of $P1$, $P2$, and S waves [60], respectively.

$$V_{P1,\,P2} = \sqrt{\frac{\lambda + 2G}{\rho_{1,\,2}}},\ V_S = \sqrt{\frac{G}{\rho}} \tag{10}$$

$$\begin{cases} \rho_{1,2} = \rho\left(d_2 \mp \sqrt{d_2^2 - d_1 d_3}\right) \\ d_1 = \frac{\lambda+2G}{Q_b} \\ d_2 = \frac{1}{2\rho}\left(\rho + \frac{\lambda+2G+\alpha^2 Q_b}{Q_b}\rho_{m1}\right) \\ d_3 = \frac{\rho_{m1}}{\rho} \end{cases} \tag{11}$$

As shown in Equation (10), all nominal wave velocities of three body waves are complex numbers, which are uniformly expressed in the following complex form:

$$V = V^r + V^i i \tag{12}$$

The real part V^r of the wave velocity in the equation represents the actual wave velocity of the wave, and the imaginary part V^i reflects the attenuation of wave. Therefore, the real part V^r of the wave velocity corresponding to the $P1$, $P2$, and S waves is the actual wave velocity of the three types of waves in saturated soil.

3. Viscous-Spring Artificial Boundary

In Figure 1, the surface of the semi-infinite saturated soil space is a free drainage boundary, and the artificial boundary Γ is introduced to divide the semi-infinite space into two parts: the interior domain Ω_{I} and the exterior domain Ω_{E}. The interior domain may have complex geometry and material properties, and convenient for solving using the finite element method. The infinite exterior domain is approximated as a uniform media of linear elasticity, and the effect of the exterior domain on the interior domain is generally achieved through artificial boundaries. For this problem, the displacement $\boldsymbol{u}$ and pore pressure p, the total stress $\boldsymbol{\sigma}$, and the fluid phase flow velocity Φ of the interior domain and exterior domain should satisfy the continuous conditions, shown as follows:

$$\begin{cases} \boldsymbol{u}_{\mathrm{I}} = \boldsymbol{u}_{\mathrm{E}} & \text{on } \Gamma_u \\ p_{\mathrm{I}} = p_{\mathrm{E}} & \text{on } \Gamma_p \\ \boldsymbol{\sigma}_{\mathrm{I}} + \boldsymbol{\sigma}_{\mathrm{E}} = 0 & \text{on } \Gamma_\sigma \\ \Phi_{\mathrm{I}} = \Phi_{\mathrm{E}} & \text{on } \Gamma_\Phi \end{cases} \tag{13}$$

where $\boldsymbol{\sigma}$ represents the total stress of soil, and Φ is the flow velocity of pore fluid in saturated soil. Therefore, the flow velocity condition and stress condition should be satisfied on the artificial boundary.

3.1. Flow Velocity Boundary Condition

The wave propagation problem under the action of a point source on the surface of the interior domain is similar to the significance of Green's function of the diffusion equation, that is, the field distribution generated by a unit point source. At the same time, the Lamb problem [61] analyzes the distribution of a variable field under the action of a concentrated force or point source on the surface of infinite space, such as pore water pressure in a saturated soil field under a point force. To obtain the pore pressure value on the artificial boundary, Green's function constructs the pore pressure field distribution of fluid-saturated porous media under the action of interior concentrated force. Therefore, Equation (2) is converted into the equation as follows in two-dimensional plane polar coordinates without considering the exterior loading and ignoring the coupling term $\alpha\nabla \cdot \dot{\boldsymbol{u}}$:

$$\frac{\partial p}{\partial t} = k_f Q_b \frac{\partial^2 p}{\partial r^2} \tag{14}$$

where r represents the outer normal direction of the artificial boundary, and t is time. It can be seen that Equation (14) is the standard form of the diffusion equation. In the infinite domain, based on Equation (14), the Green's function $G(r,t)$ [62] for the pore pressure p is obtained, and its distribution form is shown as follows:

$$p = G(r,t) = \frac{1}{4\pi k_f Q_b t} e^{-\frac{r^2}{4k_f Q \cdot t}} \tag{15}$$

By utilizing the relationship between the flow velocity and the pore pressure $\Phi = -k_f \frac{\partial p}{\partial r}$, the flow velocity boundary condition expressed in terms of pore pressure is shown below:

$$\Phi = \left(\frac{l_r}{2Q_b \cdot t}\right) p \tag{16}$$

where p and Φ are the pore pressure and the flow velocity in the outward normal direction of the artificial boundary. Since the seepage process is a time-varying diffusion process of pore fluid in saturated porous media, only when the wave propagates to the artificial boundary is there a pressure gradient between the artificial boundary and the internal domain of soil. Therefore, Equation (16) can be further written as:

$$\Phi = \begin{cases} 0 & (t < t_0) \\ \left(\frac{l_r}{2Q_b \cdot t}\right) p & (t \geq t_0) \end{cases} \tag{17}$$

where l_r is defined as the distance from the geometric center of the interior domain to the point on the artificial boundary; t_0 is the shortest time for the wave to propagate to the artificial boundary.

3.2. Stress Boundary Condition

Since Equations (8) and (9) are standard wave equations, to simplify the analysis, based on Equations (5)–(9), the outgoing wave of displacement can be assumed to be:

$$u_r(r,t) = (k_1 lw + k_2) f(v_1 t - r) \tag{18}$$

$$u_\perp(r,t) = (k_1 lw + k_2) f(v_2 t - r) \tag{19}$$

where n and $\perp$ represent the outer normal and tangent direction of the artificial boundary, respectively; u_r and the $u_\perp$ are solid phase displacement in the outer normal and tangent directions of the artificial boundary, respectively; v_1 and v_2 are the actual wave velocities in the normal and tangential of the artificial boundary, respectively; f represents the arbitrary waveform function; k_1 and k_2 represent wave numbers of attenuated and non-attenuated waves, respectively; l is the dimensional coordination factor; and $w = 1/\sqrt{r}$ represents the geometric attenuation factor.

Using the constitutive relationship and geometric relationship of the saturated two-phase porous media, the relationship between the total stress, displacement, and the pore pressure of saturated porous media is given:

$$\begin{cases} \sigma_r = \left[\lambda\left(\frac{\partial u_\perp}{\partial \perp} + \frac{\partial u_r}{\partial r}\right) - \alpha p\right] + 2G\frac{\partial u_r}{\partial r} \\ \sigma_\perp = \left[\lambda\left(\frac{\partial u_\perp}{\partial \perp} + \frac{\partial u_r}{\partial r}\right) - \alpha p\right] + 2G\frac{\partial u_\perp}{\partial \perp} \\ \tau = G\left(\frac{\partial u_\perp}{\partial r} + \frac{\partial u_r}{\partial \perp}\right) \end{cases} \tag{20}$$

where σ_r and $\sigma_\perp$ are the normal and tangential stresses of the solid-phase media, respectively; τ is the shear stress of the solid-phase media. In two dimensions, when the outgoing wave propagates along the outer normal direction of the artificial boundary, the stress at the artificial boundary, i.e., Equation (20), can be further simplified to:

$$\sigma_r = (\lambda + 2G)\frac{\partial u_r}{\partial r} - \alpha p \tag{21}$$

$$\tau = G\frac{\partial u_{\perp}}{\partial r} \tag{22}$$

Substitute Equation (18) into Equation (21) to obtain the normal stress represented by the waveform function f:

$$\sigma_r = -(\lambda + 2G)\left(k_1 l r^{-\frac{1}{2}} + k_2\right) f'(v_1 t - r) - \frac{1}{2}(\lambda + 2G) a l r^{-\frac{3}{2}} f(v_1 t - r) - \alpha p \tag{23}$$

By calculating the first derivative of Equation (18) with respect to time t, the relationship between the normal velocity and the waveform function f is obtained as follows:

$$\dot{u}_r(r,t) = c_1\left(k_1 l r^{-\frac{1}{2}} + k_2\right) f'(v_1 t - r) \tag{24}$$

Using Equations (18), (23), and (24) to eliminate the waveform function f, the relationship between the normal stress, displacement, velocity, and pore pressure is expressed as:

$$\sigma_r = -\frac{(\lambda + 2G)}{2r\left(1 + \frac{k_2}{k_1 l}\sqrt{r}\right)} u_r - \frac{(\lambda + 2G)}{v_1}\dot{u}_r - \alpha p \tag{25}$$

By introducing dimensionless parameters $A = \frac{k_2}{k_1 l}\sqrt{r}$ and $v_1 = \frac{\rho_3^2}{B} V_{P1}^n$, the normal stress boundary condition is further written as:

$$\sigma_n = -\frac{\lambda + 2G}{2l_r(1 + A)} u_r - B\rho V_{P1}^r \dot{u}_r - \alpha p \tag{26}$$

where the parameter A reflects the propagation characteristics of the outgoing wave, namely the amplitude ratio between the plane wave and the scattering wave; the parameter B represents the average wave velocity characteristics of the incident multi-sub-wave at different angles, namely, the relationship between the physical wave velocity and the apparent wave velocity. Through a large number of numerical calculations, the optimal values of A and B are obtained. $A = 0.8$, $B = 1.1$ [16].

Using a similar calculation process, the tangential stress boundary condition is shown below:

$$\tau = -\frac{G}{2l_r(1 + A)} u_{\perp} - B\rho V_S^n \dot{u}_{\perp} \tag{27}$$

where the definitions of parameters A and B are the same as in Equation (26).

3.3. Finite Element Discretization of Artificial Boundary

The artificial boundary Equations (17), (26), and (27) are written in discrete form as follows:

$$\boldsymbol{f}_{uBi}^{(l)} = -\boldsymbol{K}_{Bi}^{\infty(l)} \boldsymbol{u}_{Bi}^{(l)} - \boldsymbol{C}_{Bi}^{\infty(l)} \dot{\boldsymbol{u}}_{Bi}^{(l)} - \boldsymbol{Q}_{Bi}^{\infty(l)} p_{Bi}^{(l)} \tag{28}$$

$$f_{qBi}^{(l)} = J_{Bi}^{\infty(l)} p_{Bi}^{(l)} \tag{29}$$

where the superscript (l) represents the artificial boundary; ∞ represents the exterior domain; Bi represents the ith node on the boundary; $\boldsymbol{f}_{uBi}^{(l)}$ and $f_{qBi}^{(l)}$ are the stress and the flow velocity of the ith node on the boundary, respectively; $\boldsymbol{u}_{Bi}^{(l)}$ and $p_{Bi}^{(l)}$ are the displacement and the pore pressure of the ith node on the boundary, respectively. The variable matrices and scalar coefficients in Equations (28) and (29) are expressed in the following form:

$$\boldsymbol{K}_{Bi}^{\infty(l)} = L_i \begin{bmatrix} K_{BN}^{\infty} & 0 \\ 0 & K_{BT}^{\infty} \end{bmatrix}, \left\{ \begin{array}{l} K_{BN}^{\infty} = \frac{\lambda + 2G}{2l_r(1+A)} \\ K_{BT}^{\infty} = \frac{G}{2l_r(1+A)} \end{array} \right. \tag{30}$$

$$\boldsymbol{C}_{Bi}^{\infty(l)} = L_i \begin{bmatrix} C_{BN}^{\infty} & 0 \\ 0 & C_{BT}^{\infty} \end{bmatrix}, \left\{ \begin{array}{l} C_{BN}^{\infty} = B\rho V_{P1}^r \\ C_{BT}^{\infty} = B\rho V_S^r \end{array} \right. \tag{31}$$

$$\boldsymbol{Q}_{Bi}^{\infty(l)} = L_i \begin{bmatrix} Q_B^{\infty} \\ 0 \end{bmatrix},\ Q_B^{\infty} = \alpha \tag{32}$$

$$J_{Bi}^{\infty(l)} = L_i J_B^{\infty},\ J_B^{\infty} = \frac{l_r}{2Q_b t} \tag{33}$$

where L_i represents the boundary length corresponding to the boundary node i. Converting Equations (28) and (29) from the local coordinate system into the global coordinate system, we get:

$$\boldsymbol{f}_{uBi} = -\boldsymbol{K}_{Bi}^{\infty}\boldsymbol{u}_{Bi} - \boldsymbol{C}_{Bi}^{\infty}\dot{\boldsymbol{u}}_{Bi} - \boldsymbol{Q}_{Bi}^{\infty}p_{Bi} \tag{34}$$

$$f_{qBi} = J_{Bi}^{\infty}p_{Bi} \tag{35}$$

In Equations (34) and (35), the physical meanings of each matrix and scalar coefficient are the same as that in Equations (28) and (29), and the coordinate transformations are carried out through the following relationships:

$$\begin{cases} \boldsymbol{K}_{Bi}^{\infty} = \boldsymbol{W}^{\mathrm{T}}\boldsymbol{K}_{Bi}^{\infty(l)}\boldsymbol{W} \\ \boldsymbol{C}_{Bi}^{\infty} = \boldsymbol{W}^{\mathrm{T}}\boldsymbol{C}_{Bi}^{\infty(l)}\boldsymbol{W} \\ \boldsymbol{Q}_{Bi}^{\infty} = \boldsymbol{W}^{\mathrm{T}}\boldsymbol{Q}_{Bi}^{\infty(l)} \end{cases} \tag{36}$$

$$J_{Bi}^{\infty} = J_{Bi}^{\infty(l)} \tag{37}$$

where $\boldsymbol{W} = \begin{bmatrix} l_{rx} & l_{ry} \\ l_{\perp x} & l_{\perp y} \end{bmatrix}$ is the coordinate transformation matrix for transforming local coordinates to global coordinates. $l_{rx} = \cos(r, x)$ is the cosine of the angle between the positive direction of the local coordinate r-axis and the positive direction of the global coordinate x-axis. The rest of the parameters are similar to the definition of l_{xy}.

After discretization by the Galerkin finite element method, the dynamic governing equations of the saturated two-phase porous media, Equations (1) and (2), are represented by block matrices of internal domain and boundary:

$$\begin{bmatrix} \boldsymbol{M}_I & \boldsymbol{M}_{IB} \\ \boldsymbol{M}_{BI} & \boldsymbol{M}_B \end{bmatrix} \begin{Bmatrix} \ddot{\boldsymbol{u}}_I \\ \ddot{\boldsymbol{u}}_B \end{Bmatrix} + \begin{bmatrix} \boldsymbol{K}_I & \boldsymbol{K}_{IB} \\ \boldsymbol{K}_{BI} & \boldsymbol{K}_B \end{bmatrix} \begin{Bmatrix} \boldsymbol{u}_I \\ \boldsymbol{u}_B \end{Bmatrix} - \begin{bmatrix} \boldsymbol{Q}_I & \boldsymbol{Q}_{IB} \\ \boldsymbol{Q}_{BI} & \boldsymbol{Q}_B \end{bmatrix} \begin{Bmatrix} \boldsymbol{p}_I \\ \boldsymbol{p}_B \end{Bmatrix} = \begin{Bmatrix} \boldsymbol{f}_{uI} \\ \boldsymbol{f}_{uB} \end{Bmatrix} \tag{38}$$

$$\begin{bmatrix} \boldsymbol{S}_I & \boldsymbol{S}_{IB} \\ \boldsymbol{S}_{BI} & \boldsymbol{S}_B \end{bmatrix} \begin{Bmatrix} \dot{\boldsymbol{p}}_I \\ \dot{\boldsymbol{p}}_B \end{Bmatrix} + \begin{bmatrix} \boldsymbol{J}_I & \boldsymbol{J}_{IB} \\ \boldsymbol{J}_{BI} & \boldsymbol{J}_B \end{bmatrix} \begin{Bmatrix} \boldsymbol{p}_I \\ \boldsymbol{p}_B \end{Bmatrix} + \begin{bmatrix} \boldsymbol{Q}_I^T & \boldsymbol{Q}_{BI}^T \\ \boldsymbol{Q}_{IB}^T & \boldsymbol{Q}_B^T \end{bmatrix} \begin{Bmatrix} \dot{\boldsymbol{u}}_I \\ \dot{\boldsymbol{u}}_B \end{Bmatrix} = \begin{Bmatrix} -\boldsymbol{f}_{qI} \\ -\boldsymbol{f}_{qB} \end{Bmatrix} \tag{39}$$

where the subscripts B and I correspond to the nodes at the boundary and the internal domain, respectively; $\boldsymbol{M}$ is the mass matrix; $\boldsymbol{K}$ is the stiffness matrix; $\boldsymbol{Q}$ is the coupling matrix; $\boldsymbol{S}$ is the fluid compression matrix; $\boldsymbol{J}$ is the fluid permeability matrix. $\boldsymbol{f}_{uI}$ and $\boldsymbol{f}_{qI}$ represent the loading and fluid injection point source of the internal domain, respectively. $\boldsymbol{f}_{uB}$ and $\boldsymbol{f}_{qB}$ represent the effect of the exterior domain on the internal domain, namely the artificial boundary conditions (34) and (35), respectively.

At the same time, substituting Equations (34) and (35) into Equations (38) and (39), the finite element discrete equations of saturated porous media considering the boundary conditions are obtained:

$$\begin{bmatrix} \boldsymbol{M}_I & \boldsymbol{M}_{IB} \\ \boldsymbol{M}_{BI} & \boldsymbol{M}_B \end{bmatrix} \begin{Bmatrix} \ddot{\boldsymbol{u}}_I \\ \ddot{\boldsymbol{u}}_B \end{Bmatrix} + \begin{bmatrix} \boldsymbol{K}_I & \boldsymbol{K}_{IB} \\ \boldsymbol{K}_{BI} & \boldsymbol{K}_B + \boldsymbol{K}_B^{\infty} \end{bmatrix} \begin{Bmatrix} \boldsymbol{u}_I \\ \boldsymbol{u}_B \end{Bmatrix} + \begin{bmatrix} \boldsymbol{0} & \boldsymbol{0} \\ \boldsymbol{0} & \boldsymbol{C}_B^{\infty} \end{bmatrix} \begin{Bmatrix} \dot{\boldsymbol{u}}_I \\ \dot{\boldsymbol{u}}_B \end{Bmatrix} - \begin{bmatrix} \boldsymbol{Q}_I & \boldsymbol{Q}_{IB} \\ \boldsymbol{Q}_{BI} & \boldsymbol{Q}_B - \boldsymbol{Q}_B^{\infty} \end{bmatrix} \begin{Bmatrix} \boldsymbol{p}_I \\ \boldsymbol{p}_B \end{Bmatrix} = \begin{Bmatrix} \boldsymbol{f}_{uI} \\ \boldsymbol{0} \end{Bmatrix} \tag{40}$$

$$\begin{bmatrix} \boldsymbol{S}_I & \boldsymbol{S}_{IB} \\ \boldsymbol{S}_{BI} & \boldsymbol{S}_B \end{bmatrix} \begin{Bmatrix} \dot{\boldsymbol{p}}_I \\ \dot{\boldsymbol{p}}_B \end{Bmatrix} + \begin{bmatrix} \boldsymbol{J}_I & \boldsymbol{J}_{IB} \\ \boldsymbol{J}_{BI} & \boldsymbol{J}_B + \boldsymbol{J}_B^{\infty} \end{bmatrix} \begin{Bmatrix} \boldsymbol{p}_I \\ \boldsymbol{p}_B \end{Bmatrix} + \begin{bmatrix} \boldsymbol{Q}_I^T & \boldsymbol{Q}_{BI}^T \\ \boldsymbol{Q}_{IB}^T & \boldsymbol{Q}_B^T \end{bmatrix} \begin{Bmatrix} \dot{\boldsymbol{u}}_I \\ \dot{\boldsymbol{u}}_B \end{Bmatrix} = \begin{Bmatrix} -\boldsymbol{f}_{qI} \\ \boldsymbol{0} \end{Bmatrix} \tag{41}$$

where $\boldsymbol{K}_B^{\infty}$, $\boldsymbol{C}_B^{\infty}$, $\boldsymbol{Q}_B^{\infty}$, and $\boldsymbol{J}_B^{\infty}$ are calculated by Equations (36) and (37), respectively. The finite element discrete equations of saturated porous media can be calculated by different time domain integration methods. The proposed artificial boundary actually only changes the values of the corresponding boundary nodes on the diagonal of the coefficient matrices in Equations (40) and (41). The finite element discrete equations of saturated porous media considering the boundary conditions can be solved by a completely explicit integration algorithm efficiently, which is shown in Appendix A.

The proposed artificial boundary has a simple form and is easily applied to the finite element method. Since the boundary has a local approximate form both in the space and time domains, it has low computational cost and high computational efficiency. Effective calculation accuracy can be guaranteed when the artificial boundary is set at a sufficient distance from the internal source.

4. Numerical Studies

4.1. Example 1

The computational model of one-dimensional saturated soil is shown in Figure 2. Both lateral sides of the model are fixed impermeable boundaries. The top surface is a permeable boundary and is applied a uniform constant loading of 1.0 Pa. The models (a)–(c) have different bottom boundaries, such as remote boundary, fixed boundary, and artificial boundary, respectively. For the model (a), the truncated boundary is set far enough away from the load center, and within the effective calculation time, the reflected wave generated by the boundary cannot propagate to the concerned calculation area. The numerical solutions of the model (a) can be used as reference solutions for comparison. For model (b) and model (c), the truncation boundaries have the same distance from the load center and are much closer than the remote boundary. However, the truncation boundary of model (b) is a fixed boundary, while the truncated boundary of model (c) is set to the proposed artificial boundary. The material parameters of the model, taken from Simon [63] are shown in Table 1 for the values of Material 1. The analytical solutions of the one-dimensional problem of saturated soil proposed by Simon [63] are used as the reference solution and are compared with the results of the remote boundary and the fixed boundary to verify the correctness of the artificial boundary proposed in this paper.

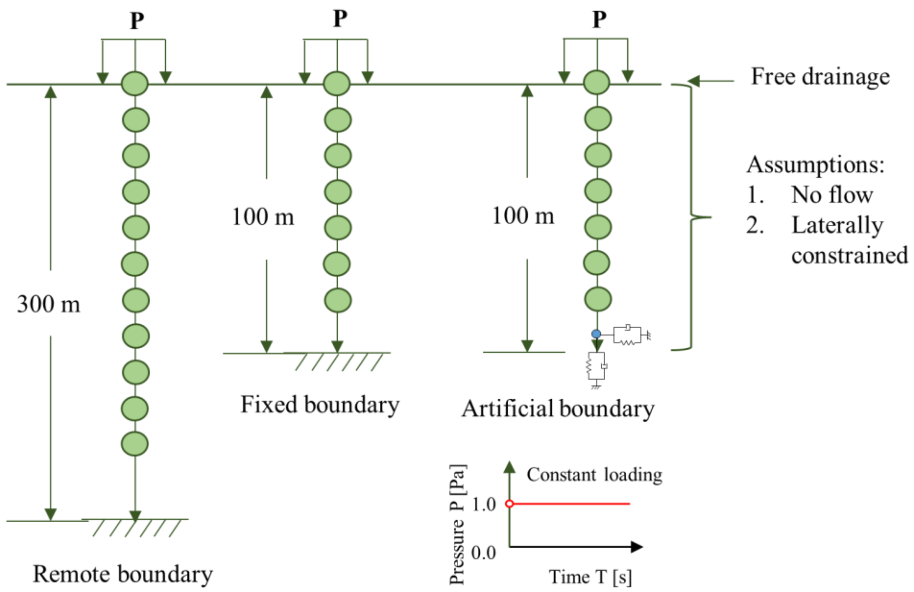

Figure 2. One-dimensional model of fluid-saturated porous media.

Table 1. Material parameters of the linear elastic saturated soil.

Parameter	Value		
E_S	3000 Pa		Young's modulus
R	0.306 kg/m^3		Density of two-phase media
ρ_f	0.2977 kg/m^3		Density of pore fluid
n_p	0.333		Porosity
C	0.2		Poisson's ratio
k_f	0.004883 m^{3}s/kg		Dynamic permeability coefficient
L	833.3 Pa		Lame constant
G	1250 Pa		Modulus of shear
Material Number	**Value 1**	**Value 2**	
K_f	0.3999×10^5 Pa	0.6106×10^5 Pa	Pore fluid volume modulus
Ks	∞	0.5005×10^4 Pa	Solid-phase soil skeleton volume modulus
Q_b	0.1201×10^6 Pa	0.1385×10^5 Pa	Pore fluid compressibility coefficient
	Wave Velocity		
Actual Wave Velocity	**Material No.**		
	1	**2**	
C_p	635.12 m/s	176.15 m/s	P wave velocity
C_s	63.92 m/s	63.92 m/s	S wave velocity

The time-history responses of nodes 5 m and 45 m away from the load center are, respectively, selected for comparison. The time-history results of the displacement and pore pressure calculated by the three models are shown in Figure 3. It can be seen from the figure that the analytical solutions and the calculation results of the far boundary are almost completely resumed. Both results are used as the reference solutions. However, the difference between the responses of the fixed boundary and the reference solution is large, indicating that the bottom fixed boundary produces an unreal reflected wave propagating to the target node, which affects the real responses of the node. The vertical displacements and pore pressure of the model with the proposed boundary are consistent with the reference solutions, which verifies the correctness of the proposed boundary. Although the pore pressure response of the node at 5 m depth from the soil surface has some oscillations at the initial stage of the calculation, the oscillation gradually decreases as time goes on.

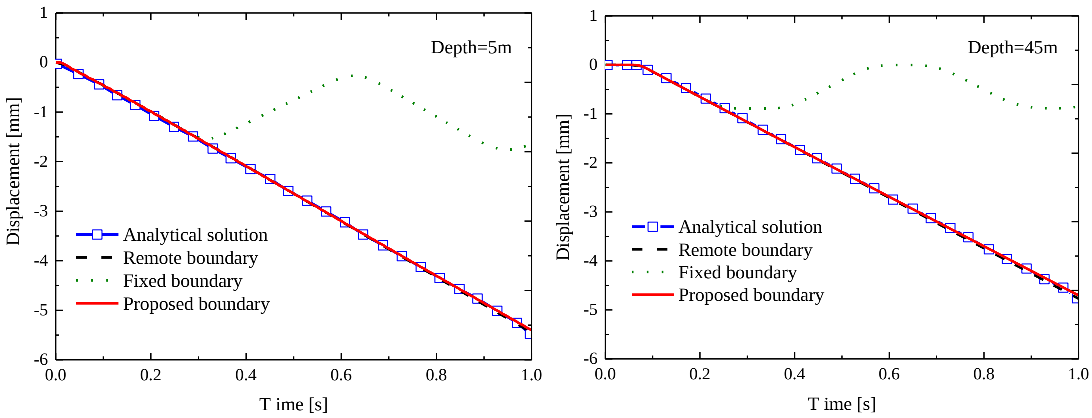

Figure 3. *Cont.*

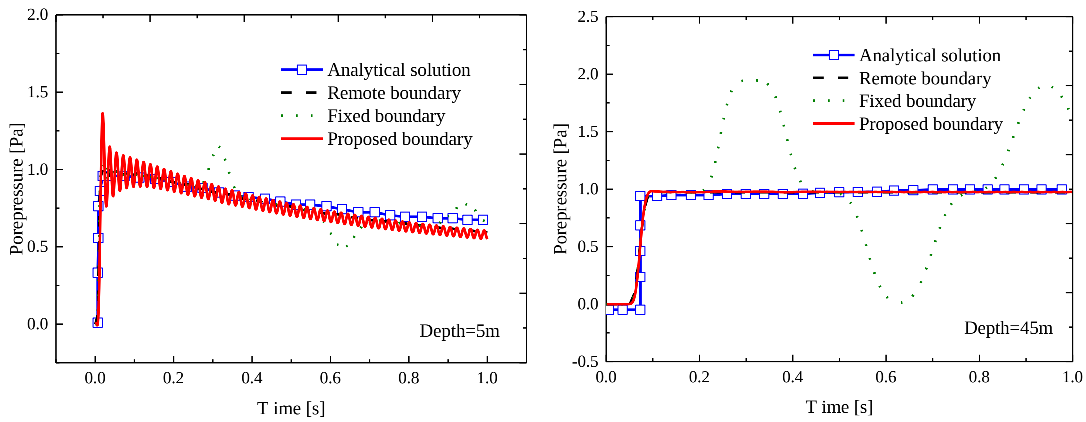

Figure 3. Vertical displacement and pore pressure time histories of one-dimensional saturated soil model.

4.2. Example 2

The calculation model of saturated soil in two-dimensional semi-infinite space is shown in Figure 4. A semi-infinite domain model including the calculation domain with an intercepted area of 20 m $\times$ 20 m, as shown in Figure 4b. The top surface of the model is the drainage boundary and is loaded with locally uniform sine loading. The viscous spring boundaries proposed by Liu et al. [51], the remote boundary, fixed boundary, and paraxial boundary proposed by Akiyoshi et al. [48], as well as the boundary proposed in this paper, are respectively applied at the intercepted boundary. By comparing with the results of the artificial boundaries mentioned above, the accuracy and advantages of the proposed boundary are illustrated. The position of the remote boundary is selected according to the following method as an example. During the time 2.0 s of the sine loading, namely, the whole calculation time, the wave propagates at the faster velocity of P wave in the soil and is reflected by the remote boundaries. However, the reflected wave is not transmitted to the node of interest within the calculation time. The locations of the remote boundaries are set at the minimum computational domain range that does not affect the dynamic responses of the interest nodes. The material parameters in the example refer to Simon [63] and are shown in Table 1 for the values of Material No. 2.

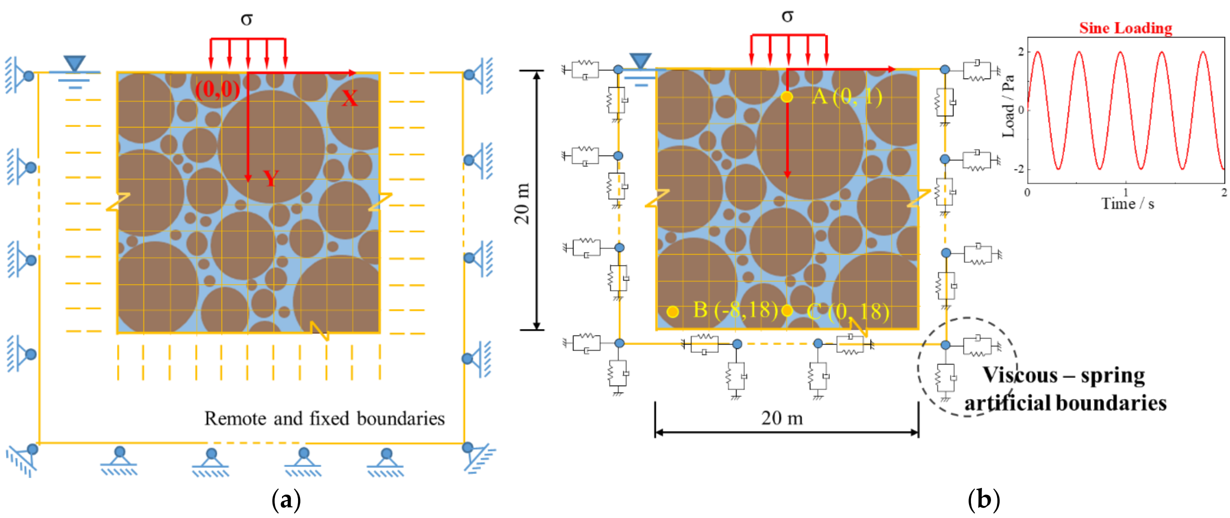

Figure 4. Two-dimensional saturated soil model under sine loading: (**a**) Model with remote and fixed boundaries; (**b**) Model with viscous–spring boundaries.

In Figure 5, taking the numerical results of the model using the remote boundary as the reference solution, the displacement and pore pressure time histories of the fixed boundary are far from the results of the reference solution. The calculation results of the proposed boundary, the paraxial boundary, and the existing viscous spring boundaries [51] are in good agreement with the reference solutions. Moreover, the proposed boundary is more accurate than the viscous spring boundary [51], which shows the accuracy of the artificial boundary proposed in this paper.

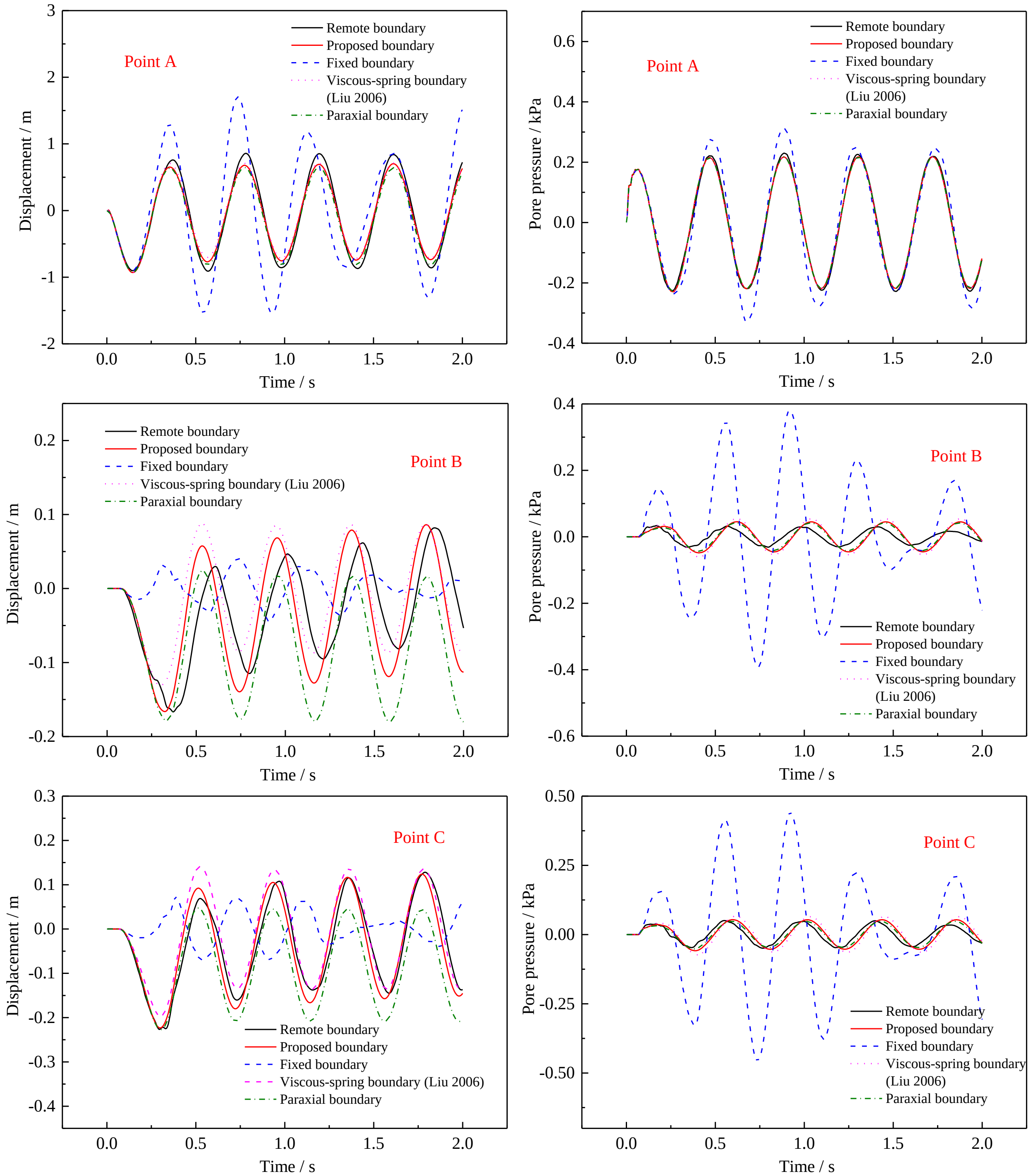

Figure 5. Vertical displacement and pore pressure time histories of the two-dimensional model with different boundaries [51].

Under the same calculation conditions and calculation method in time domain, the total computational times of the models with different boundaries mentioned above are shown in Figure 6. Among them, when the time step of the paraxial boundary is set to 5×10^{-4} s, the calculation does not converge. In the case of the remote boundary, the element number of the model is 4000, and the calculation time is 5841.81 s. Comparing several boundaries, the proposed boundary takes the shortest calculation time, which is 65.01 s. It can be seen that the proposed method has significant advantages in shortening the calculation time and improving the calculation efficiency.

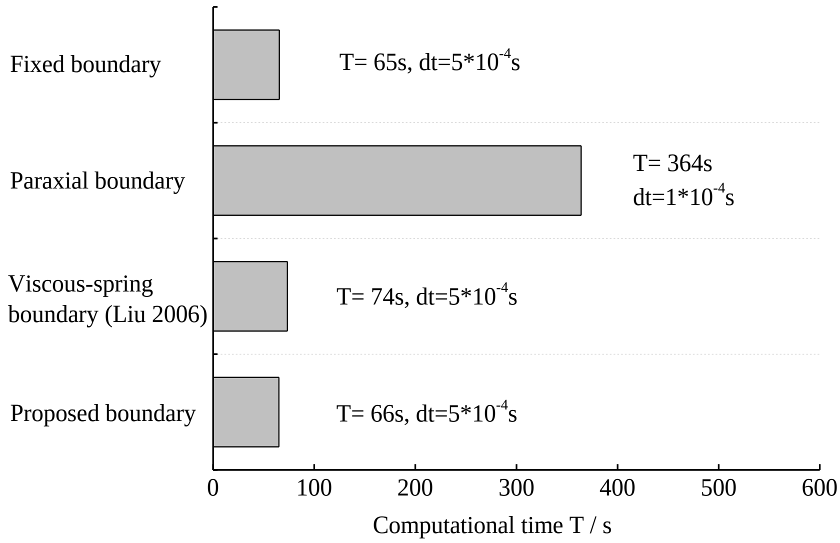

Figure 6. Comparison of computational time [51].

4.3. Example 3

The development of displacement and pore pressure of saturated soil changed under point loading is analyzed by Example 3. A concentrated impulse loading acted on the free-draining surface of the computational model, as shown in Figure 7, and an area of 20 m $\times$ 20 m is intercepted by three different boundary conditions, namely the proposed boundary, the viscous spring boundary [51] and the fixed boundary. The changes of displacement and pore pressure in the calculation area at different time points are analyzed. Moreover, the correctness of the proposed method is further verified by comparing the three boundary conditions.

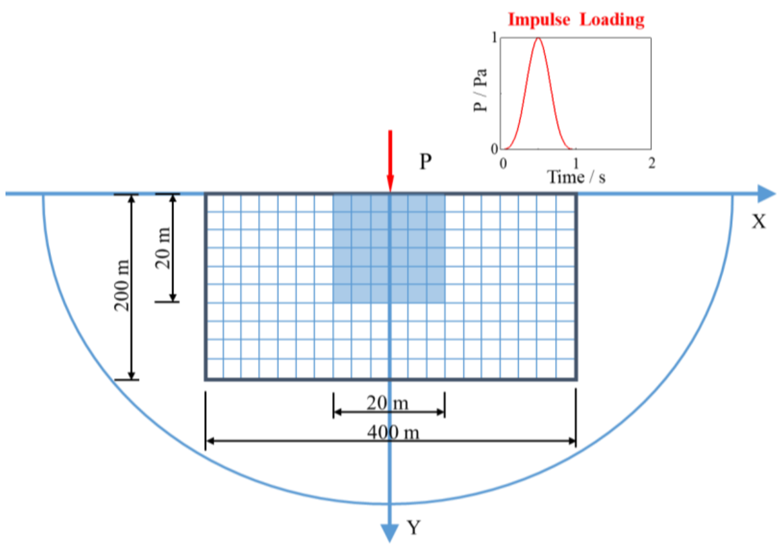

Figure 7. Computational model under impulsive loading.

Figures 8 and 9 show the distribution of displacement and pore pressure under three boundary conditions at 0.2 s, 0.5 s, and 1.0 s, respectively. From the figures, it can be seen that the influence area under the impulsive loading continues to increase with the calculation time. The formed displacement and pore pressure field continue to spread out from the point loading, and the displacement and pore pressure reach the maximum value at 0.5 s, which is the peak time of the impulsive loading. By comparing the numerical results of computational models considering the three kinds of boundary conditions, the numerical results of the proposed boundary and viscous spring boundary are the same, but the displacement and pore pressure results of the fixed boundary are completely different from that of the viscous spring boundaries. The forms of boundary conditions have a greater impact on the results of the interior domain.

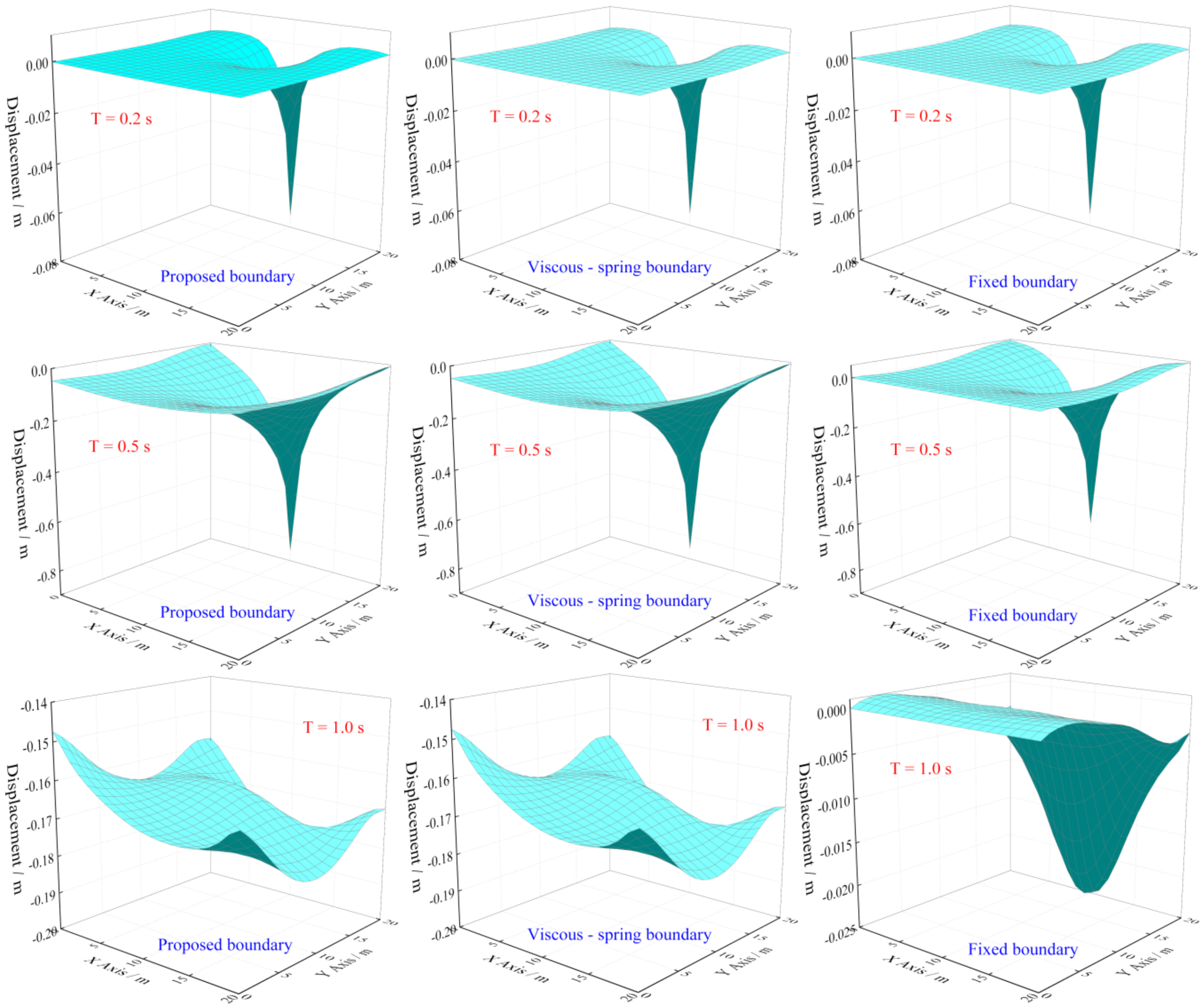

Figure 8. Comparison of displacement at different time.

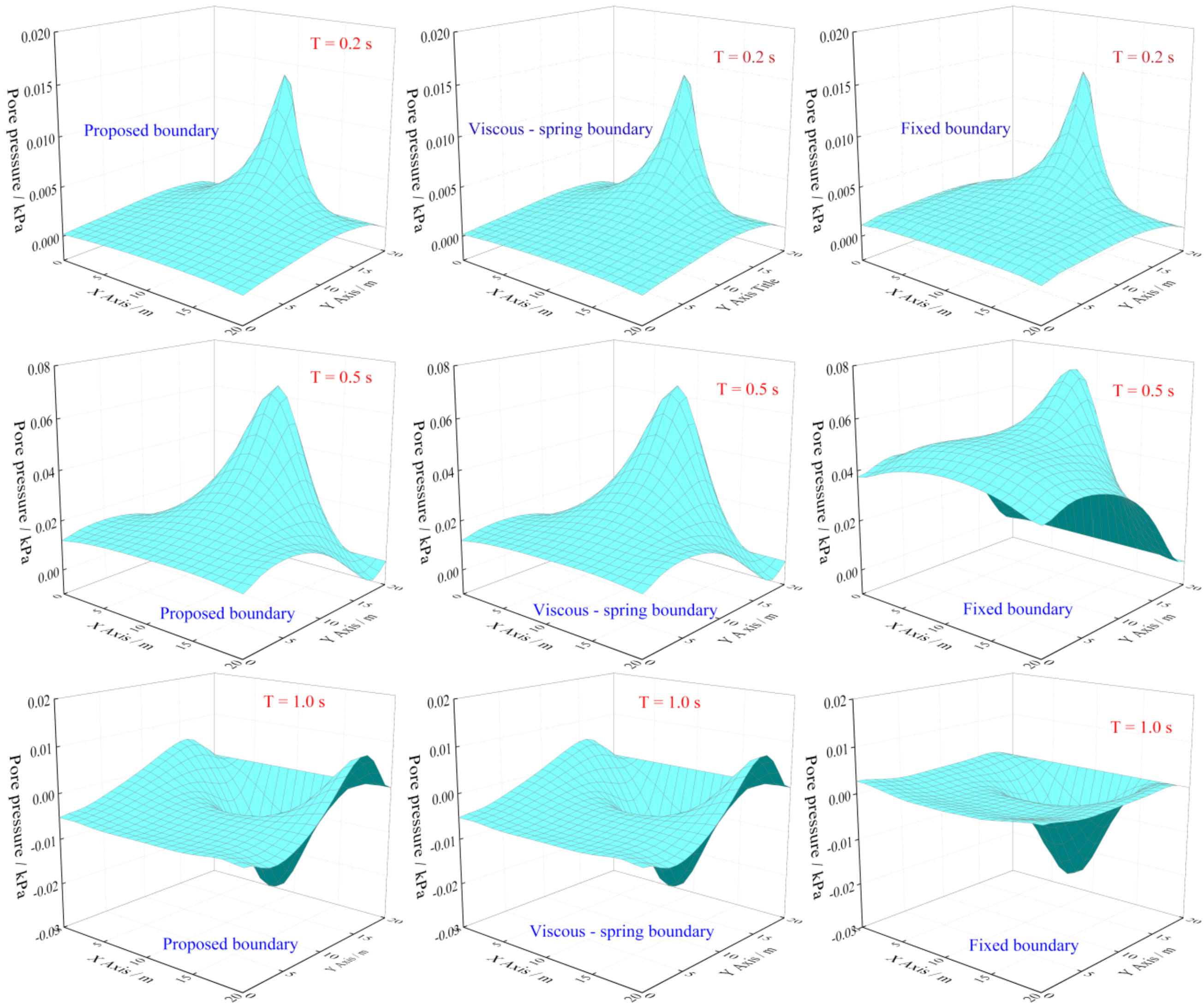

Figure 9. Comparison of pore pressure at different time.

5. Conclusions

For the energy radiation problem caused by the finite processing of the infinite model, a viscous spring boundary is proposed for the fluid-saturated porous media. The proposed method is illustrated the computational advantages and accuracy by theoretical method and numerical computation.

1. The viscous spring boundary is composed of the stress and flow velocity boundary conditions, which are constructed by the reasonable outgoing wave assumption and Green's function. The boundary has a simple form and clear physical meaning. Since the overall system equations considering artificial boundaries only need to change the values of the corresponding boundary nodes on the diagonal of the coefficient matrices, the boundary can be easily applied to the finite element method.
2. Without the assumption of permeability and using the real wave velocity, the proposed boundary has higher accuracy than the existing boundaries with the assumption of impermeability.
3. After considering the viscous spring boundary, the computational system is expressed as lumped mass equations with damping. A complete explicit integration algorithm with second-order accuracy is constructed to solve the equations.

The proposed method can be used to analyze the saturated soil-structure dynamic interaction in finite domain efficiently. The artificial boundary controls the number of degrees of freedom of the site model, and the explicit method considering the damping term also improves the calculation efficiency.

Author Contributions: Methodology, J.S.; software, J.S.; Writing—original draft, F.W.; Writing—review & editing, K.J. and H.S. All authors have read and agreed to the published version of the manuscript.

Funding: This research was funded by [National Natural Science Foundation of China] grant number [51808006], [Natural Science Foundation of Beijing] grant number [8192012], and [Yuyou Team Training Program of North China University of Technology] grant number [10751360022XN699].

Acknowledgments: The authors would like to thank the National Natural Science Foundation of China (Grant No. 51808006), the Natural Science Foundation of Beijing, China (Grant No. 8192012), and Yuyou Team Training Program of North China University of Technology (Grant No. 10751360022XN699) for funding the work presented in this paper.

Conflicts of Interest: The authors declare no conflict of interest.

Appendix A

Explicit Integration Algorithm

To simplify the analysis process, Equations (40) and (41) can be further written as follows:

$$\widetilde{\boldsymbol{M}}\ddot{\widetilde{\boldsymbol{u}}} + \widetilde{\boldsymbol{K}}\widetilde{\boldsymbol{u}} + \widetilde{\boldsymbol{C}}\dot{\widetilde{\boldsymbol{u}}} - \widetilde{\boldsymbol{Q}}_1\widetilde{\boldsymbol{p}} = \widetilde{\boldsymbol{f}}_u \tag{A1}$$

$$\widetilde{\boldsymbol{S}}\dot{\widetilde{\boldsymbol{p}}} + \widetilde{\boldsymbol{J}}\widetilde{\boldsymbol{p}} + \widetilde{\boldsymbol{Q}}_2^T\dot{\widetilde{\boldsymbol{u}}} = -\widetilde{\boldsymbol{f}}_q \tag{A2}$$

where

$$\begin{gathered}\widetilde{\boldsymbol{M}} = \begin{bmatrix} \boldsymbol{M}_I & \boldsymbol{M}_{IB} \\ \boldsymbol{M}_{BI} & \boldsymbol{M}_B \end{bmatrix}, \widetilde{\boldsymbol{K}} = \begin{bmatrix} \boldsymbol{K}_I & \boldsymbol{K}_{IB} \\ \boldsymbol{K}_{BI} & \boldsymbol{K}_B + \boldsymbol{K}_B^\infty \end{bmatrix}, \widetilde{\boldsymbol{C}} = \begin{bmatrix} \boldsymbol{0} & \boldsymbol{0} \\ \boldsymbol{0} & \boldsymbol{C}_B^\infty \end{bmatrix}, \widetilde{\boldsymbol{S}} = \begin{bmatrix} \boldsymbol{S}_I & \boldsymbol{S}_{IB} \\ \boldsymbol{S}_{BI} & \boldsymbol{S}_B \end{bmatrix} \\ \widetilde{\boldsymbol{Q}}_1 = \begin{bmatrix} \boldsymbol{Q}_I & \boldsymbol{Q}_{IB} \\ \boldsymbol{Q}_{BI} & \boldsymbol{Q}_B - \boldsymbol{Q}_B^\infty \end{bmatrix}, \widetilde{\boldsymbol{Q}}_2 = \begin{bmatrix} \boldsymbol{Q}_I & \boldsymbol{Q}_{IB} \\ \boldsymbol{Q}_{BI} & \boldsymbol{Q}_B \end{bmatrix}, \widetilde{\boldsymbol{J}} = \begin{bmatrix} \boldsymbol{J}_I & \boldsymbol{J}_{IB} \\ \boldsymbol{J}_{BI} & \boldsymbol{J}_B + \boldsymbol{J}_B^\infty \end{bmatrix}\end{gathered} \tag{A3}$$

$$\ddot{\widetilde{\boldsymbol{u}}} = \begin{Bmatrix} \ddot{\boldsymbol{u}}_I \\ \ddot{\boldsymbol{u}}_B \end{Bmatrix}, \dot{\widetilde{\boldsymbol{u}}} = \begin{Bmatrix} \dot{\boldsymbol{u}}_I \\ \dot{\boldsymbol{u}}_B \end{Bmatrix}, \widetilde{\boldsymbol{u}} = \begin{Bmatrix} \boldsymbol{u}_I \\ \boldsymbol{u}_B \end{Bmatrix}, \dot{\widetilde{\boldsymbol{p}}} = \begin{Bmatrix} \dot{\boldsymbol{p}}_I \\ \dot{\boldsymbol{p}}_B \end{Bmatrix}, \widetilde{\boldsymbol{p}} = \begin{Bmatrix} \boldsymbol{p}_I \\ \boldsymbol{p}_B \end{Bmatrix}, \widetilde{\boldsymbol{f}}_u = \begin{Bmatrix} \boldsymbol{f}_{uI} \\ \boldsymbol{0} \end{Bmatrix}, \widetilde{\boldsymbol{f}}_q = \begin{Bmatrix} \boldsymbol{f}_{qI} \\ \boldsymbol{0} \end{Bmatrix} \tag{A4}$$

There is a damping term $\widetilde{\boldsymbol{C}}\dot{\widetilde{\boldsymbol{u}}}$ in Equation (A1). Based on the explicit algorithm [64] for single-phase medium and the Euler predictor-corrector method [65], the explicit integration algorithm for two-phase media is constructed. The computational process in one time step Δt is shown as follows:

(a) The whole of the loading time is divided into several time intervals with a time step Δt, and any time can be expressed as $t_k = t_{k-1} + \Delta t$, ($k = 1, 2, 3, \ldots$). Equation (A1) is solved using the explicit algorithm method [64] to obtain the step-by-step recurrence formula of the solid phase displacement $\widetilde{\boldsymbol{u}}_{k+1}$ at the time t_{k+1}:

$$\widetilde{\boldsymbol{u}}_{k+1} = \left(\boldsymbol{I} - \frac{\Delta t^2}{2}\widetilde{\boldsymbol{M}}^{-1}\widetilde{\boldsymbol{K}} + \frac{\Delta t}{2}\widetilde{\boldsymbol{M}}^{-1}\widetilde{C}\right)\widetilde{\boldsymbol{u}}_k - \frac{\Delta t}{2}\widetilde{\boldsymbol{M}}^{-1}\widetilde{C}\widetilde{\boldsymbol{u}}_{k-1} + \left(\Delta t - \Delta t^2\widetilde{\boldsymbol{M}}^{-1}\widetilde{C}\right)\dot{\widetilde{\boldsymbol{u}}}_k + \frac{\Delta t^2}{2}\widetilde{\boldsymbol{M}}^{-1}\widetilde{\boldsymbol{Q}}\widetilde{\boldsymbol{p}}_k + \frac{\Delta t^2}{2}\widetilde{\boldsymbol{M}}^{-1}\widetilde{\boldsymbol{f}}_{uk} \tag{A5}$$

(b) To express the acceleration $\ddot{\widetilde{\boldsymbol{u}}}_k$ at the time t_k, convert Equation (A1) into the following form:

$$\ddot{\widetilde{\boldsymbol{u}}}_k = \widetilde{\boldsymbol{M}}^{-1}\left(\widetilde{\boldsymbol{f}}_{uk} - \widetilde{\boldsymbol{K}}\widetilde{\boldsymbol{u}}_k - \widetilde{\boldsymbol{C}}\dot{\widetilde{\boldsymbol{u}}}_k + \widetilde{\boldsymbol{Q}}\widetilde{\boldsymbol{p}}_k\right) \tag{A6}$$

(c) Apply the Newmark method to get the velocity $\dot{\tilde{\boldsymbol{u}}}_{k+1}$ at the time t_{k+1}. The parameters $\beta = 0.25$, $\gamma = 0.5$

$$\dot{\tilde{\boldsymbol{u}}}_{k+1} = \frac{\gamma}{\beta \Delta t}\left[\tilde{\boldsymbol{u}}_{k+1} - \tilde{\boldsymbol{u}}_k\right] + \left(1 - \frac{\gamma}{\beta}\right)\dot{\tilde{\boldsymbol{u}}}_k + \left(1 - \frac{\gamma}{2\beta}\right)\Delta t \ddot{\tilde{\boldsymbol{u}}}_k \tag{A7}$$

where $\tilde{\boldsymbol{u}}_{k+1}$, $\tilde{\boldsymbol{u}}_k$, $\dot{\tilde{\boldsymbol{u}}}_k$, and $\ddot{\tilde{\boldsymbol{u}}}_k$ are known items.

(d) Equation (A2) is solved using the Euler predictor-corrector method [65]. The formulas are shown as follows:

$$\bar{\bar{\boldsymbol{p}}}_{k+1} = \left(\boldsymbol{I} - \Delta t \tilde{\boldsymbol{S}}^{-1} \tilde{\boldsymbol{J}}\right)\tilde{\boldsymbol{p}}_k - \Delta t \tilde{\boldsymbol{S}}^{-1} \tilde{\boldsymbol{Q}}^T \dot{\tilde{\boldsymbol{u}}}_k + \Delta t \tilde{\boldsymbol{S}}^{-1} \tilde{\boldsymbol{f}}_{qk} \tag{A8}$$

$$\tilde{\boldsymbol{p}}_{k+1} = \left(\boldsymbol{I} - \frac{\Delta t}{2}\tilde{\boldsymbol{S}}^{-1}\tilde{\boldsymbol{J}}\right)\tilde{\boldsymbol{p}}_k - \frac{\Delta t}{2}\tilde{\boldsymbol{S}}^{-1}\tilde{\boldsymbol{J}}\bar{\bar{\boldsymbol{p}}}_{k+1} - \frac{\Delta t}{2}\tilde{\boldsymbol{S}}^{-1}\tilde{\boldsymbol{Q}}^T\dot{\tilde{\boldsymbol{u}}}_k - \frac{\Delta t}{2}\tilde{\boldsymbol{S}}^{-1}\tilde{\boldsymbol{Q}}^T\dot{\tilde{\boldsymbol{u}}}_{k+1} + \frac{\Delta t}{2}\tilde{\boldsymbol{S}}^{-1}\left(\tilde{\boldsymbol{f}}_{qk} + \tilde{\boldsymbol{f}}_{q(k+1)}\right) \tag{A9}$$

The predictor value firstly is calculated using Equation (A8), and then the predictor value $\bar{\bar{\boldsymbol{p}}}_{k+1}$ and known variable $\dot{\tilde{\boldsymbol{u}}}_{k+1}$, which is obtained by Equation (A7), are substituted into Equation (A9) to calculate the corrector value, that is, the pore pressure $\tilde{\boldsymbol{p}}_{k+1}$ at the time t_{k+1}.

To sum up, Equations (A5)–(A9) represent the integration algorithm of the lumped-mass equations with damping. The algorithm is a completely explicit algorithm with second-order accuracy.

References

1. Biot, M.A. General theory of three-dimensional consolidation. *J. Appl. Phys.* **1941**, *12*, 155–164. [CrossRef]
2. Biot, M.A. Theory of propagation of elastic waves in a fluid-saturated porous solid. I. Low-frequency range. *J. Acoust. Soc. Am.* **1956**, *28*, 168–178. [CrossRef]
3. Biot, M.A. Theory of propagation of elastic waves in a fluid-saturated porous solid. II. Higher frequency range. *J. Acoust. Soc. Am.* **1956**, *28*, 179–191. [CrossRef]
4. Lévy, T. Propagation of waves in a fluid-saturated porous elastic solid. *Int. J. Eng. Sci.* **1979**, *17*, 1005–1014. [CrossRef]
5. Auriault, J.L. Dynamic behaviour of a porous medium saturated by a Newtonian fluid. *Int. J. Eng. Sci.* **1980**, *18*, 775–785. [CrossRef]
6. Prevost, J.H. Nonlinear transient phenomena in saturated porous media. *Comput. Methods Appl. Mech. Eng.* **1982**, *30*, 3–18. [CrossRef]
7. Zienkiewicz, O.C.; Shiomi, T. Dynamic behaviour of saturated porous media; the generalized Biot formulation and its numerical solution. *Int. J. Numer. Anal. Methods Geomech.* **1984**, *8*, 71–96. [CrossRef]
8. Zienkiewicz, O.C.; Chan, A.H.C.; Pastor, M.; Schrefler, B.A.; Shiomi, T. *Computational Geomechanics with Special Reference to Earthquake Enineering*; John Wiley & Sons: New York, NY, USA, 1998.
9. Men, F.L. Wave propagation in fluid-saturated porous media. *Acta Geophys.* **1981**, *24*, 65–75. (In Chinese)
10. Chen, L.Z.; Wu, S.M.; Zeng, G.X. Propagation of elastic waves in saturated soil. *Acta Mech.* **1987**, *19*, 276–283. (In Chinese)
11. Wu, S.M. *Waves in Soil*; Science Press: Beijing, China, 1997. (In Chinese)
12. Zhao, C.G.; Du, X.L.; Cui, J. Advances in wave theory and numerical simulation in solid and fluid multiphase porous media. *Adv. Mech.* **1998**, *28*, 83–91. (In Chinese)
13. Morency, C.; Tromp, J. Spectral-element simulations of wave propagation in porous media. *Geophys. J. Int.* **2008**, *175*, 301–345. [CrossRef]
14. De la Puente, J.; Dumbser, M.; Käser, M.; Igel, H. Discontinuous Galerkin methods for wave propagation in poroelastic media. *Geophysics* **2008**, *73*, T77–T97. [CrossRef]
15. Wang, Y.F.; Liang, J.W.; Chen, A.L.; Wang, Y.S.; Laude, V. Evanescent waves in two-dimensional fluid-saturated porous metamaterials with a transversely isotropic matrix. *Phys. Rev. B* **2020**, *101*, 184301. [CrossRef]
16. Zhao, M. *A Comparative Study of Viscoelastic Artificial Boundaries and Their Transmission Artificial Boundaries*; Beijing University of Technology: Beijing, China, 2004. (In Chinese)
17. Zhao, M.; Du, X.L.; Liu, J.B.; Liu, H. Explicit finite element artificial boundary scheme for transient scalar waves in two-dimensional unbounded waveguide. *Int. J. Numer. Methods Eng.* **2011**, *87*, 1074–1104. (In Chinese) [CrossRef]
18. Teng, Z.H. Exact boundary condition for time-dependent wave equation based on boundary integral. *J. Comput. Phys.* **2003**, *190*, 398–418. (In Chinese) [CrossRef]
19. Givoli, D.; Cohen, D. Nonreflecting Boundary Conditions Based on Kirchhoff-Type Formulae. *J. Comput. Phys.* **1995**, *117*, 102–113. [CrossRef]

20. Givoli, D. Exact Representations on Artificial Interfaces and Applications in Mechanics. *Appl. Mech. Rev.* **1999**, *52*, 333–349. [CrossRef]
21. Lysmer, J.; Kuhlemeyer, R.L. Finite dynamic model for infinite media. *J. Eng. Mech. Div.* **1969**, *95*, 859–878. [CrossRef]
22. Deeks, A.J.; Randolph, M.F. Axisymmetric time-domain transmitting boundaries. *J. Eng. Mech.* **1994**, *120*, 25–42. [CrossRef]
23. Kellezi, L. Local transmitting boundaries for transient elastic analysis. *Soil Dyn. Earthq. Eng.* **2000**, *19*, 533–547. [CrossRef]
24. Liu, J.B.; Du, Y.; Du, X.L.; Wang, Z.; Wu, J. 3D viscous-spring artificial boundary in time domain. *Earthq. Eng. Eng. Vib.* **2006**, *5*, 93–102. (In Chinese) [CrossRef]
25. Smith, W.D. A nonreflecting plane boundary for wave propagation problems. *J. Comput. Phys.* **1974**, *15*, 492–503. [CrossRef]
26. Liao, Z.P.; Wong, H.L. A transmitting boundary for the numerical simulation of elastic wave propagation. *Int. J. Soil Dyn. Earthq. Eng.* **1984**, *3*, 174–183. (In Chinese) [CrossRef]
27. Higdon, R.L. Radiation boundary conditions for elastic wave propagation. *SIAM J. Numer. Anal.* **1990**, *27*, 831–869. [CrossRef]
28. Hall, W.S.; Oliveto, G. *Boundary Element Methods for Soil-Structure Interaction*; Springer Science and Business Media: Berlin/Heidelberg, Germany, 2003.
29. Kausel, E. Thin-layer method: Formulation in the time domain. *Int. J. Numer. Methods Eng.* **1994**, *37*, 927–941. [CrossRef]
30. Givoli, D. Recent advances in the DtN FE method. *Arch. Comput. Methods Eng.* **1999**, *6*, 71–116. [CrossRef]
31. Kuhlemeyer, R.L.; Lysmer, J. Finite element method accuracy for wave propagation problems. *J. Soil Mech. Found. Div.* **1973**, *99*, 421–427. [CrossRef]
32. Du, X.L. Locally decoupled time domain wave analysis method. *World Earthq. Eng.* **2000**, *16*, 22–26. (In Chinese)
33. Du, X.L.; Zhao, M.; Wang, J.T. Artificial stress boundary strips for near-field wave simulation. *Acta Mech.* **2006**, *38*, 49–56. (In Chinese)
34. Li, P.; Song, E.X. A high-order time-domain transmitting boundary for cylindrical wave propagation problems in unbounded saturated poroelastic media. *Soil Dyn. Earthq. Eng.* **2013**, *48*, 48–62. (In Chinese) [CrossRef]
35. Liu, J.B.; Lu, Y. A direct method for analysis of dynamic soil-structure interaction based on interface idea. *Dev. Geotech. Eng.* **1998**, *83*, 261–276. (In Chinese)
36. Kunar, R.R.; Marti, J. Computational methods for infinite domain media-structure interaction. *J. Appl. Mech. Div.* **1981**, *46*, 183–204.
37. Liao, Z.P. Extrapolation non-reflecting boundary conditions. *Wave Motion* **1996**, *24*, 117–138. (In Chinese) [CrossRef]
38. Clayton, R.; Engquist, B. Absorbing boundary conditions for acoustic and elastic wave equations. *Bull. Seism. Soc. Am.* **1977**, *67*, 1529–1540. [CrossRef]
39. Engquist, B.; Majda, A. Radiation boundary conditions for acoustic and elastic wave calculations. *Commun. Pure Appl. Math.* **1979**, *32*, 313–357. [CrossRef]
40. Higdon, R.L. Numerical absorbing boundary conditions for the wave equation. *Math. Comput.* **1987**, *49*, 65–90. [CrossRef]
41. Komatitsch, D.; Martin, R. An unsplit convolutional perfectly matched layer improved at grazing incidence for the seismic wave equation. *Geophysics* **2007**, *72*, SM155–SM167. [CrossRef]
42. Zeng, Y.Q.; He, J.Q.; Liu, Q.H. The application of the perfectly matched layer in numerical modeling of wave propagation in poroelastic media. *Geophysics* **2001**, *66*, 1258–1266. (In Chinese) [CrossRef]
43. Zhao, C.; Valliappan, S. A dynamic infinite element for three-dimensional infinite-domain wave problems. *Int. J. Numer. Methods Eng.* **1993**, *36*, 2567–2580. [CrossRef]
44. Zhao, C. *Dynamic and Transient Infinite Elements: Theory and Geophysical, Geotechnical and Geoenvironmental Applications*; Springer Science & Business Media: Berlin/Heidelberg, Germany, 2009.
45. Zhao, C. Coupled method of finite and dynamic infinite elements for simulating wave propagation in elastic solids involving infinite domains. *Sci. China Technol. Sci.* **2010**, *53*, 1678–1687. [CrossRef]
46. Modaressi, H.; Benzenati, I. An absorbing boundary element for dynamic analysis of two-phase media. In Proceedings of the 10th World Conference on Earthquake Engineering, Madrid, Spain, 19–24 July 1992; pp. 1157–1163.
47. Modaressi, H.; Benzenati, I. Paraxial approximation for poroelastic media. *Soil Dyn. Earthq. Eng.* **1994**, *13*, 117–129. [CrossRef]
48. Akiyoshi, T.; Fuchida, K.; Fang, H. Absorbing boundary conditions for dynamic analysis of fluid-saturated porous media. *Soil Dyn. Earthq. Eng.* **1994**, *13*, 387–397. [CrossRef]
49. Akiyoshi, T.; Fang, H.L.; Fuchida, K.; Matsumoto, H. A non-linear seismic response analysis method for saturated soil-structure system with absorbing boundary. *Int. J. Numer. Anal. Methods Géoméch.* **1996**, *20*, 307–329. [CrossRef]
50. Akiyoshi, T.; Sun, X.; Fuchida, K. General absorbing boundary conditions for dynamic analysis of fluid-saturated porous media. *Soil Dyn. Earthq. Eng.* **1998**, *17*, 397–406. [CrossRef]
51. Liu, G.L.; Song, E.X. Viscoelastic transport boundary of numerical simulation of saturated infinite foundation. *Chin. J. Geotech. Eng.* **2006**, *28*, 2128–2133. (In Chinese)
52. Du, X.L.; Li, L.Y. A Viscoelastic Artificial Boundary for Near-Field Fluctuation Analysis of Saturated Porous Media. *Chin. J. Geophys.* **2008**, *51*, 575–581. (In Chinese)
53. Wang, Z.H.; Zhao, C.G.; Dong, L. An approximate spring dashpot artificial boundary for transient wave analysis of fluid-saturated porous media. *Comput. Geotech.* **2009**, *36*, 199–210. (In Chinese) [CrossRef]
54. Wang, G.J.; Zhao, C.G. Artificial boundary of viscoelastic dynamics of fluid saturated porous media. *World Seismol. Eng.* **2007**, *23*, 54–59. (In Chinese)

55. Li, P.; Song, E.X. A viscous-spring transmitting boundary for cylindrical wave propagation in saturated poroelastic media. *Soil Dyn. Earthq. Eng.* **2014**, *65*, 269–283. (In Chinese) [CrossRef]
56. Degrande, G.; De Roeck, G. An absorbing boundary condition for wave propagation in saturated poroelastic media—Part I: Formulation and efficiency evaluation. *Soil Dyn. Earthq. Eng.* **1993**, *12*, 411–421. [CrossRef]
57. Degrande, G.; De Roeck, G. An absorbing boundary condition for wave propagation in saturated poroelastic media—Part II: Finite element formulation. *Soil Dyn. Earthq. Eng.* **1993**, *12*, 423–432. [CrossRef]
58. Gajo, A.; Saetta, A.; Vitaliani, R. Silent boundary conditions for wave propagation in saturated porous media. *Int. J. Numer. Anal. Methods Geomech.* **1996**, *20*, 253–273. [CrossRef]
59. Zerfa, Z.; Loret, B. A viscous boundary for transient analyses of saturated porous media. *Earthq. Eng. Struct. Dyn.* **2003**, *33*, 89–110. [CrossRef]
60. Song, J. *Wave Numerical Method of Saturated Soil Site and Its Engineering Application*; Beijing University of Technology: Beijing, China, 2012. (In Chinese)
61. Philippacopoulos, A.J. Lamb's problem for fluid-saturated, porous media. *Bull. Seismol. Soc. Am.* **1988**, *78*, 908–923.
62. Passty, G.B.; Haberman, R. Elementary Applied Partial Differential Equations with Fourier Series and Boundary Value Problems. *Am. Math. Mon.* **1985**, *92*, 441. [CrossRef]
63. Simon, B.R.; Zienkiewicz, O.C.; Paul, D.K. An analytical solution for the transient response of saturated porous elastic solids. *Int. J. Numer. Anal. Methods Géoméch.* **1984**, *8*, 381–398. [CrossRef]
64. Du, X.L.; Wang, J.T. An explicit difference formulation of dynamic response calculation of elastic structure with damping. *Eng. Mech.* **2000**, *17*, 37–43.
65. Xue, Y. *Numerical Analysis and Scientific Computing*; Science Press: Beijing, China, 2011; pp. 355–363. (In Chinese)